Single-Crystal Capacitive Sensors with Micropatterned Electrodes via Space-Confined Growth of the Metal–Organic Framework HKUST-1

Benzheng Xia, Aleksander Matavž, Min Tu, Víctor Rubio-Giménez, Max Lutz Tietze, João Marreiros, Frederik Ceyssens, Charlotte Cresens, Nathalie Wauteraerts, Alexey Kubarev, Michael Kraft, and Rob Ameloot**

The polyhedral shape and fragile nature of single crystals of metal–organic frameworks (MOFs) hinder their processing using standard microfabrication techniques. As a result, the fabrication of surface patterns and microelectrodes on MOF single crystals is challenging, which limits both the direct electrical interrogation of crystals in research and their integration into optical and electrical devices. Herein, a new strategy to readily fabricate surface-embossed micropatterns and surface-embedded gold electrodes on MOF single crystals using a space-confined, one-step solvothermal synthesis is demonstrated. This method is based on the confined growth of the MOF crystal around prefabricated metal patterns with different adhesion strengths to the growth surface, producing features as small as 5 µm. As a proof of concept, micropatterns are created on flat single crystals of the MOF HKUST-1, exhibiting the function as a diffraction grating. Additionally, a single-crystal HKUST-1 capacitive gas sensor with surface-embedded electrodes that serves as a stable platform for the investigation of ethanol diffusion in the MOF pores is fabricated. The space-confined fabrication strategy is promising for the integration of fragile MOF single crystals in various optical and electrical devices.

1. Introduction

Metal–organic frameworks (MOFs) are porous materials that consist of metal nodes connected by organic linkers to produce highly ordered structures with various pore geometries and chemical properties.[1,2] As a result of their unique and tunable structure, MOFs have shown promise in a wide range of applications, including gas adsorption and separation,[3–5] catalysis,[6,7] nanomedicine,[8] and sensing.[9,10] To investigate the intrinsic properties of MOFs, single crystals are ideal platforms that mitigate the impact of defects, impurities, and grain boundaries that exist in polycrystalline films.[11,12] However, integrating MOF single crystals into devices and interrogating them electrically, either for material characterization or for practical application, is challenging because of the following reasons. First, most MOF single crystals exhibit a polyhedral morphology, which is incompatible with the typically planar architecture of optical and electronic devices. Second, the fragile nature of MOF single crystals raises the risk of damage during processing using standard microfabrication techniques.

To bridge this gap and obtain a more suitable morphology, one strategy involves cutting MOF single crystals using techniques like electron-beam and X-ray lithography.[13,14] However, these techniques are complex and sparsely accessible. An alternative approach is space-confined synthesis, in which

B. Xia, A. Matavž, V. Rubio-Giménez, M. L. Tietze, J. Marreiros, N. Wauteraerts, A. Kubarev, R. Ameloot
Center for Membrane Separations
Adsorption
Catalysis, and Spectroscopy (cMACS)
KU Leuven
3001 Leuven, Belgium
E-mail: rob.ameloot@kuleuven.be

M. Tu
State Key Laboratory of Transducer Technology
Shanghai Institute of Microsystem and Information Technology
Chinese Academy of Sciences
Shanghai 200050, China

M. Tu
2020 X-Lab
Shanghai Institute of Microsystem and Information Technology
Chinese Academy of Sciences
Shanghai 200050, China
E-mail: min.tu@mail.sim.ac.cn

F. Ceyssens, M. Kraft
Micro- and Nano Systems (MNS)
KU Leuven
3001 Leuven, Belgium

C. Cresens
Department of Chemistry
KU Leuven
3001 Leuven, Belgium

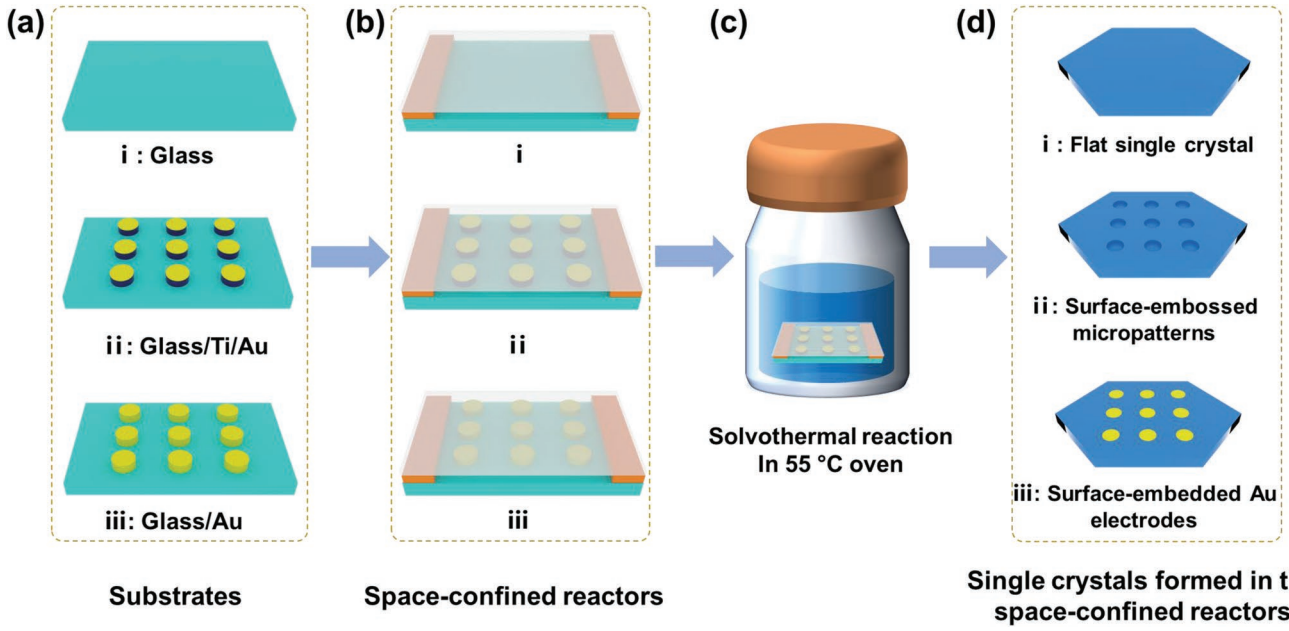

Scheme 1. Schematic illustration of the space-confined synthesis of HKUST-1 single crystals with three types of morphology features. a) Three substrates used in the synthesis include: i) a flat glass substrate and glass substrates with ii) Ti/Au, and iii) Au patterns. b) Space-confined reactors were formed by assembling two spacers (Kapton tape) between the substrate and a cover glass. c) The space-confined reactor was immersed in a precursor solution for the solvothermal synthesis of HKUST-1 single crystals. d) The resulting HKUST-1 single crystals include i) flat single crystals and single crystals with ii) surface-embossed micropatterns and iii) surface-embedded gold electrodes.

the growth of the single crystals is guided by a narrow gap between two surfaces. This method is productively used to synthesize perovskite single-crystal films and has the advantages of easy processing and maintaining the material properties.[15–20] However, examples of the space-confined synthesis of MOFs single crystals are scarce.[21–24] Flat, high-aspect-ratio HKUST-1 single crystals have been synthesized using soft lithography and nanofluidic channels.[24,25] Additionally, despite one demonstration of surface nanopatterning on a perovskite single crystal film,[26] most space-confined synthesis methods can only obtain single crystals with flat surfaces. The low diversity of surface morphologies limits the optical and electrical properties of single crystals.[26,27]

Wiring up the fragile crystals is crucial to the integration of MOF single crystals into electrical devices.[28] Previous reports of MOF single-crystal-based electrical devices have either suffered from low-precision electrode contacts or the requirement of complex electrode deposition techniques. For instance, attaching metal wires onto a single crystal with conductive paste is a simple yet crude approach for achieving electrode contact. The shape of the conduction channel between the electrodes is typically irregular, thus prompting errors in calculating the device's electrical properties, especially for miniaturized devices.[28] Alternatively, bonding the single crystal to prefabricated electrodes via electron-beam-induced metal deposition has been utilized to form a more regular conduction channel.[29] However, this technique is costly and time-consuming. Direct electron-beam lithography combined with thermal metal deposition can fabricate precise electronic devices on quasi-/2D MOF single crystals.[11,21] Nevertheless, this method requires exposure of the MOF to chemicals (photoresist and developer) and harsh conditions (metal thermal deposition in high vacuum), increasing the risk of damaging or contaminating the fragile and porous single crystals. In addition, transfer printing has been reported to deposit electrodes on organic single crystals.[30,31] However, this contact procedure risks damaging the crystals through and the need for a donor substrate adds an extra layer of complexity.

In this work, we report a modified space-confined approach to synthesizing flat MOF single crystals with surface-embossed micropatterns and surface-embedded gold electrodes using a one-step solvothermal reaction (**Scheme 1**). In contrast with the flat, unpatterned growth surfaces typically used in space-confined synthesis, glass substrates with pre-fabricated titanium/gold (Ti/Au) and Au patterns were used. The Ti/Au patterns function as impregnable barriers that guide the growth of the MOF single crystal, resulting in surface-embossed micropatterns upon removal of the MOF crystal. In contrast, without the Ti adhesion layer, the Au patterns detach from the glass substrate and embed into the flat MOF single crystal. To demonstrate this concept, we chose the MOF HKUST-1 (also known as copper-benzene-1, 3, 5-tricarboxylate, CuBTC), which possesses unsaturated Cu^{2+} sites, and has been extensively studied as a gas sensing material.[32,33] With our approach, surface micropatterns and Au electrode arrays with feature sizes down to 5 μm were fabricated on flat HKUST-1 single crystals. The surface-embossed micropatterns show potential as diffraction gratings. The HKUST-1 single crystal with surface-embedded interdigitated electrodes functions as a capacitive gas sensor, which was used to investigate the diffusion of ethanol molecules into the MOF.

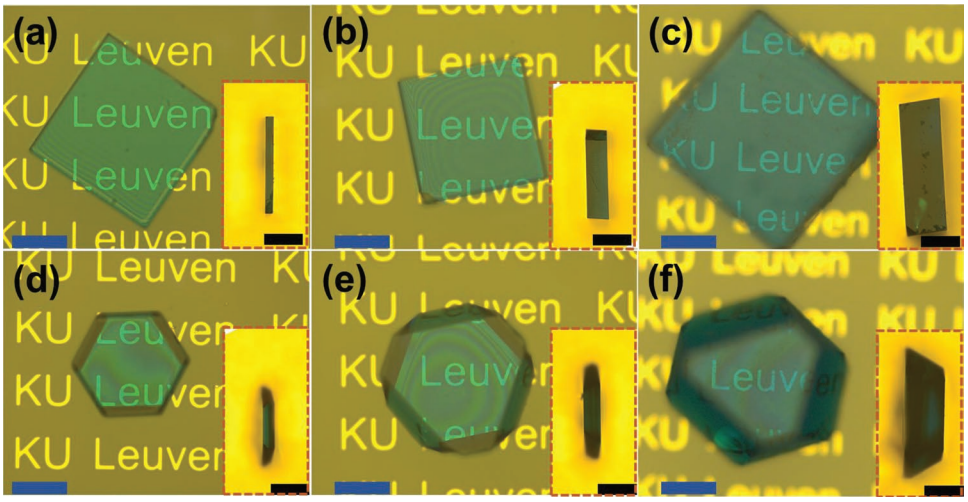

Figure 1. Micrographs of HKUST-1 flat single crystals with different thicknesses and crystallographic orientations: a–c), [100] oriented; d–f) [111] oriented. The single crystals are placed on a glass substrate with Au patterns to demonstrate their transparency. The thicknesses of the crystals can be controlled by the thickness of the spacer, which was 10 µm for (a,d), 20 µm for (b,e), and 40 µm for (c,f). Scale bar (blue) = 100 µm. Insets: the micrographs of the side view of the corresponding HKUST-1 flat single crystals. Scale bar (black) = 40 µm.

2. Results and Discussion

2.1. Space-Confined Synthesis of HKUST-1 Single Crystals

Scheme 1 shows the synthesis of three types of HKUST-1 single crystals via the space-confined solvothermal reaction (cross-sectional illustration in Scheme S1, Supporting Information). To achieve different surface features on HKUST-1 single crystals, three different substrates are employed, including flat glass, flat glass with Ti/Au patterns, and flat glass with pure Au patterns (Scheme 1a, see the Experimental Section for fabrication details). The corresponding space-confined reactors are formed by placing two spacers (i.e., Kapton tape) on each glass substrate, and then sandwiched with a cover glass (Scheme 1b). The entire assembly is then submerged into a precursor solution to synthesize HKUST-1 (Scheme 1c, see the Experimental Section for details).[34] The precursor solution fills the space-confined reactor, where nucleation and growth of the single crystal occurs. After synthesis, the substrate and cover glass are separated to pick the resulting single crystals inside the reactor for further characterization (Scheme 1d).

The physical constraints of the presented reactor design guide crystal growth along the lateral direction as soon as it reaches the opposite glass surface. As a result, flat single crystals of HKUST-1 are formed in the confined space, the thickness of which is determined by the distance between the two glass slides. More interestingly, when a glass substrate with a patterned surface was employed, these patterns could be replicated on the contact surface of the single crystal (Figure S1, Supporting Information). This approach offers a solution to the issue of fabricating microstructures on the surface of fragile MOF single crystals. Therefore, more precise Ti/Au patterns (Scheme 1a(ii)) were fabricated on the growth surface of the space-confined reactor, acting as impregnable barriers to emboss elaborate surface patterns on the HKUST-1 single crystals (Scheme 1d(ii)). Furthermore, given the weak adhesion between Au and glass without the Ti adhesive layer, the Au layer (Scheme 1a(iii)) detaches from the glass substrate together with the HKUST-1 crystal, producing surface-embedded gold patterns (Scheme 1d(iii)).

2.2. HKUST-1 Flat Single Crystals

Flat single crystals of HKUST-1 with thicknesses ranging from 10 to 40 µm (**Figure 1**; Figure S2, Supporting Information) were obtained via the space-confined synthesis by adjusting the thickness of the spacer. All crystals exhibited high optical transparency (Figure 1), which is beneficial for optical applications.[35,36] Each flat single crystal features a dominant crystallographic orientation, which can be identified via the crystal shape (Figure 1; Figure S3a,b, Supporting Information), in contrast to the typical polyhedral shape obtained from the unconfined synthesis (Figure S3c, Supporting Information). Specifically, the square and hexagonal shapes represent flat single crystals of [100] and [111]-oriented HKUST-1, respectively, as confirmed by X-ray diffraction (XRD).[33,37] As shown in **Figure 2**a, only two diffraction peaks at $2\theta = 6.6°$ and 13.2° were recorded for square HKUST-1 single crystals (Figure 2b), corresponding to the (200) and (400) diffractions of HKUST-1. In comparison, only peaks corresponding to the [111] crystallographic orientation were observed in the XRD pattern of the hexagonal HKUST-1 single crystal (Figure 2c). The position of each peak is identical to the simulated XRD patterns of HKUST-1 along the [100] and [111] crystallographic orientations, respectively (Figure 2a).[33] Both dominant orientations can form in the same space-confined reactor, indicating a non-preferred crystallization of the MOF.

2.3. HKUST-1 Flat Single Crystals with Surface-Embossed Micropatterns

When the glass substrates with Ti/Au patterns were employed in the space-confined reactor, the single crystals would grow

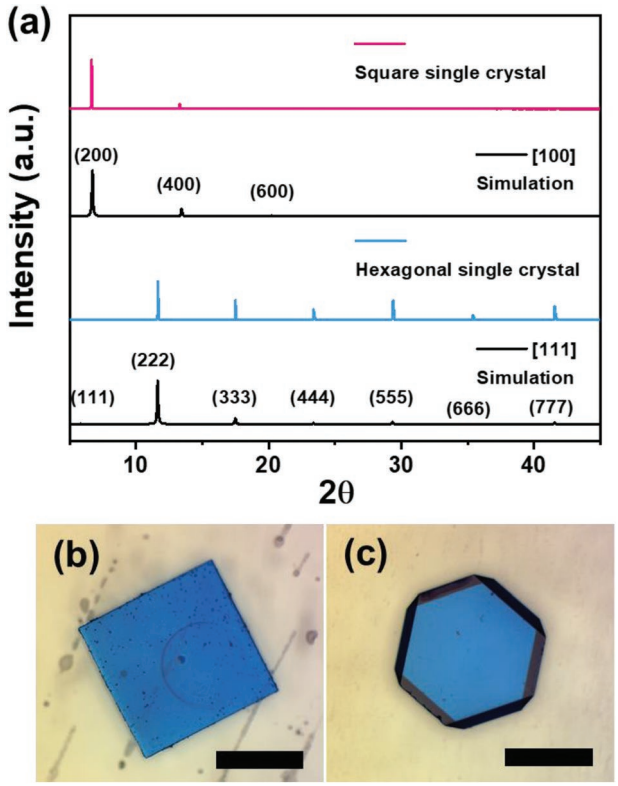

Figure 2. Experimental and simulated XRD patterns of the [100] and [111] crystallographic orientations of HKUST-1. The experimental XRD patterns in (a) are obtained from the square and hexagonal HKUST-1 flat single crystals shown in (b) and (c), respectively. Scale bar: 250 μm.

around these features. Upon removal of the substrate after the space-confined synthesis, the Ti/Au features remain adhered to the glass substrate, resulting in a surface-embossed pattern in the MOF single crystal. As an example, a surface-embossed square pattern with a side length of 10 μm (**Figure 3**a–c) and depth of ≈230 nm (Figure 3d) was demonstrated, measured by optical profilometry. This micropatterning approach enables sophisticated geometries, such as dots, long stripes, and hexagrams of different heights and depths (Figures S4 and S5, Supporting Information). Additionally, surface-embossed micropatterns can be produced on both sides of a HKUST-1 flat single crystal by fabricating Ti/Au patterns on both the bottom substrate and cover glass of the space-confined reactor (Figure S6, Supporting Information). The potential of the surface-embossed micropatterns to function as a diffraction grating is demonstrated in Figure S7a (Supporting Information). Various diffraction patterns are generated when 561 nm laser light shines through flat single crystals with surface-embossed dots (Figure S7b,d,f, Supporting Information) and parallel stripes (Figure S7c,e,g, Supporting Information).

2.4. HKUST-1 Flat Single Crystals with Surface-Embedded Au Electrodes

The ability of the space-confined synthesis to deposit surface-embedded electrodes on HKUST-1 single crystals was also explored by taking advantage of the weak adhesion between Au and the glass substrate. Circular Au electrode arrays with diameters ranging from 5 to 100 μm were patterned on the substrate, followed by the space-confined growth of HKUST-1 single

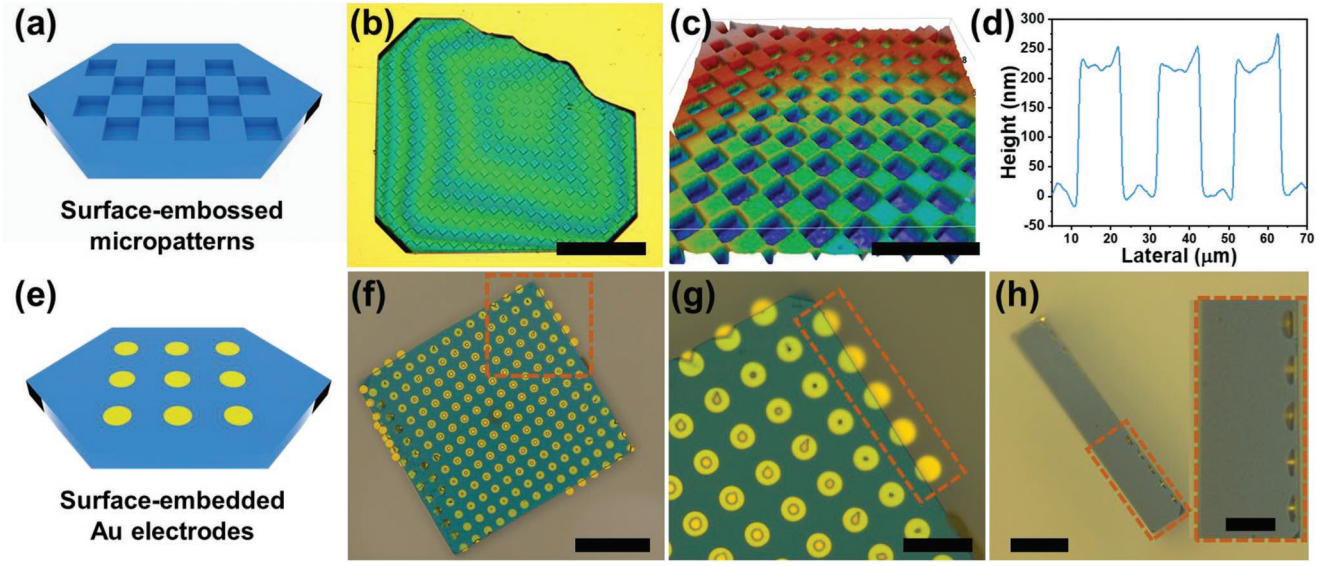

Figure 3. HKUST-1 flat single crystals with surface-embossed micropatterns and surface-embedded gold electrodes. a) Schematic illustration, b) optical micrograph, and c) 3D optical profilometry of a flat single crystal HKUST-1 with surface-embossed micropatterns, d) height profile of the periodic square patterns measured via 3D optical profilometry. The side length and embossed depth of the squares are 10 μm and 230 nm, respectively. e) Schematic illustration and f) optical micrograph of an HKUST-1 flat single crystal with surface-embedded gold electrodes. The diameter of each Au electrode is 10 μm. g) Zoomed-in micrograph of the surface-embedded gold electrodes in (f). h) The side-view of crystal in (f), inset: zoomed-in side-view of the highlighted area (red dashed square) in (g) and (h). Scale bars of 100 μm for (b), (f), 30 μm for (c), (g), and 60 μm for (h), 20 μm for the inset of (h).

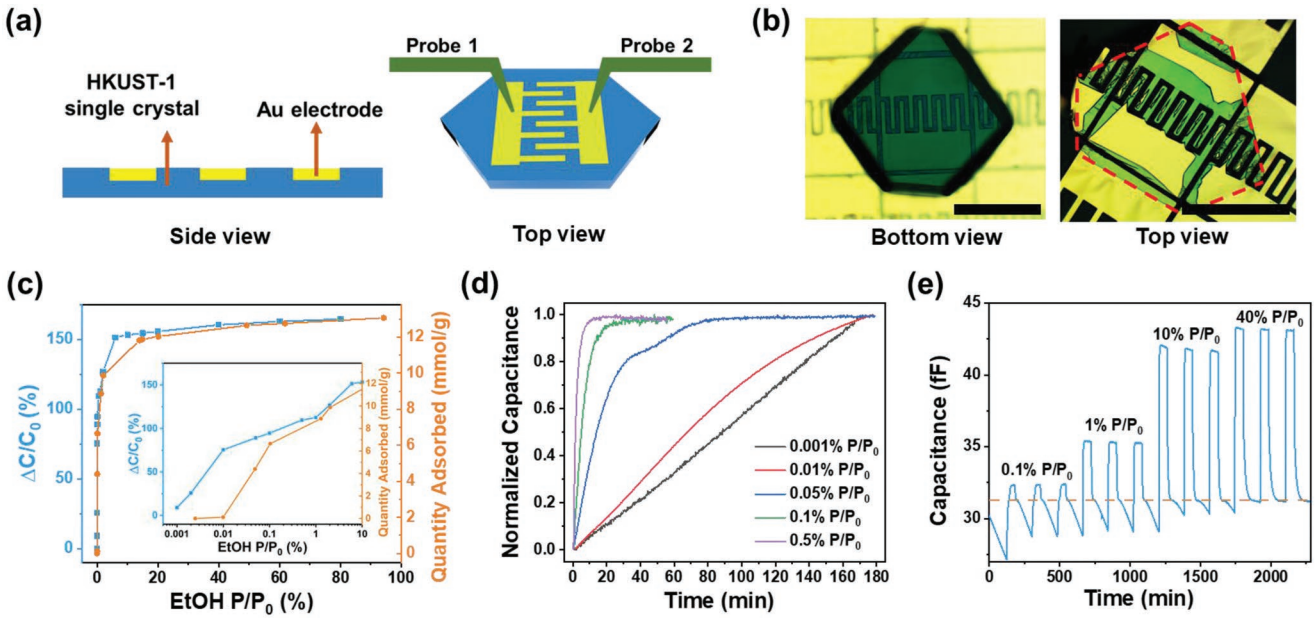

Figure 4. HKUST-1 single-crystal capacitive gas sensor with surface-embedded interdigitated electrodes and its sensing performance to ethanol vapor. a) Schematic diagrams showing the side and top view of the HKUST-1 single-crystal capacitive gas sensor. Two probes are used to contact the surface-embedded interdigitated electrodes to monitor the capacitance of the HKUST-1 single crystal. b) Optical micrographs showing the bottom and top views of the HKUST-1 single crystal capacitive gas sensor. Scale bar: 200 µm. c) The relative capacitive response ($\Delta C/C_0$) of the single-crystal HKUST-1 gas sensor as a function of the ethanol vapor pressure (P/P_0), and the ethanol adsorption isotherm of the HKUST-1 powder sample. Inset: the linear-log graph of the $\Delta C/C_0$ from 0.001% to 10% P/P_0 of ethanol vapor. d) The normalized capacitance changes as a function of equilibration time under different ethanol vapor pressures. e) The repeatable response of the sensor to different ethanol vapor pressures.

crystals. Upon completing the synthesis, detachment of the Au electrodes from the glass substrate was observed, as these remained embedded in the HKUST-1 single crystals (Figure 3e–g; Figure S8, Supporting Information). Because the Au electrodes were pre-fabricated on the substrate and transferred to the single crystal during synthesis, no visible damage to the fragile MOF crystal was induced (Figure S9, Supporting Information). In contrast, the HKUST-1 single crystal was completely destroyed upon the attempts to fabricate surface electrodes by sputter-deposition through a shadow mask (Figure S10, Supporting Information). Interestingly, the embedded Au electrodes were found to be partially or completely covered by the crystal (Figure 3g,h; Figure S8, Supporting Information), indicating the Au patterns detached before the crystal growth ceased. The same phenomenon was also observed on a zinc-based MOF, ZIF-8.[38,39] Partially covered Au electrodes were embedded on ZIF-8 single crystals (Figure S11, Supporting Information). Therefore, we hypothesize that during the space-confined MOF growth, the Au motifs are tightly encircled by the crystal, identical to the formation of the surface-embossed patterns. However, due to the weak adhesion between the Au and glass substrate, the crystal gradually intrudes into this interface, eventually causing the Au patterns detached from the glass. Subsequently, the single crystal continues to grow, partially or fully covering the electrodes.

2.5. HKUST-1 Single-Crystal Gas Sensor

Taking advantage of the fabrication strategy, a proof-of-concept capacitive gas sensor was designed by embedding an interdigitated Au electrode structure (dimensions in Figure S12, Supporting Information) into a HKUST-1 flat single crystal (**Figure 4**a). Two probes were used to contact the surface-embedded electrodes to monitor the capacitance of the HKUST-1 crystal. By embedding the electrodes in the MOF, rather than growing the MOF over surface-anchored electrodes, the parasitic contribution of the substrate to the measured capacitance was eliminated, enabling a low C_0 value (Figure S13, Supporting Information).[40] As a result, changes induced by analyte adsorption in the MOF crystal can be detected with a higher sensitivity (vide infra). Figure 4b shows optical microscopy images of the resulting sensor, demonstrating a non-defective HKUST-1 single crystal from the bottom view and the surface-embedded interdigitated electrode on the single crystal from the top view. As with the partially covered circular Au electrodes, some parts of the interdigitated electrode are covered by HKUST-1.

Before gas sensing measurements, activation of the MOF crystal is required. However, the typical thermal activation process is not suitable as the HKUST-1 flat single crystals were cracked even upon modest baking at 50 °C (Figure S14d, Supporting Information). In addition, direct N_2 purging to exchange the air (45% relative humidity) in the measurement cell can instantly destroy the single crystal structure (Figure S15, Supporting Information). The collapse of the single crystal can be explained by the shrinkage of the HKUST-1 unit cell upon removing the coordinated water molecules on the Cu^{2+} sites.[41,42] In contrast, HKUST-1 exhibited better stability through ethanol sorption cycles, attributing to the relatively lower interaction energy between ethanol and the Cu^{2+} sites.[43] Therefore, we first exposed the HKUST-1 single-crystal gas

sensor to ethanol vapor (40% P/P_0) for 10 min to exchange the adsorbed moisture, followed by N_2 purging to remove the adsorbed ethanol. However, due to the coordination with Cu^{2+} sites, ethanol could not be completely removed at room temperature,[43] even after 26 h of N_2 purging (Figure S16, Supporting Information).

The sensing performance of the HKUST-1 single-crystal device is evaluated as the relative capacitive response $\Delta C/C_0$,[10] in which C_0 is the capacitance after 26 h of N_2 purging (see the Experimental Section for details), and ΔC is the capacitance change upon ethanol adsorption. The sensor shows a response to ethanol vapor at a concentration as low as 0.001% P/P_0 (0.6 ppm) (Figure S17, Supporting Information). The $\Delta C/C_0$ response to ethanol vapor is well in line with the ethanol adsorption isotherm determined by a volumetric measurement of the HKUST-1 powder sample (Figure 4c; Figure S18, Supporting Information). Impressively, the single-crystal device shows equilibrium $\Delta C/C_0$ values of ≈90% and ≈165% for 0.05% and 80% P/P_0 of ethanol vapor, respectively, which are outstanding relative capacitive responses for MOF-based capacitive gas sensors,[44] and HKUST-1-based gas sensors (Table S3, Supporting Information).

The HKUST-1 single-crystal gas sensor exhibited a significant difference in response time upon exposure to different ethanol concentrations (Figure 4d; Figure S17, Supporting Information). An apparent transition from a slow to a fast response at 0.05% P/P_0 was observed. Specifically, it took >3 h for the capacitance to rise from 10% to 90% of the equilibrium response for 0.01% P/P_0 and only ≈12 min for 0.1% P/P_0 of ethanol vapor (Figure 4d). The ethanol uptake of powder HKUST-1 at 0.05% P/P_0 was determined to be 4.4 mmol g^{-1} by volumetric measurement (Figure 4c), corresponding to 0.9 ethanol molecules per Cu^{2+} site. Therefore, we rationalize the slow diffusion of ethanol at low concentrations in HKUST-1 by the coordination between ethanol and the Cu^{2+} sites, which adds a activation energy for diffusion in the MOF pores. When the P/P_0 is higher than 0.05%, all Cu^{2+} sites are occupied by ethanol molecules, leading to less interactions along the diffusion path.[45,46] When the P/P_0 is between 10% and 80%, the diffusion completes within 2 min (Table S1, Supporting Information), in agreement with previous reports.[47] The coordination of ethanol to Cu^{2+} also explains the extremely slow desorption process. Specifically, the inflection point, indicating the transition from fast desorption to slow desorption, was observed at a capacitance of 31.5 fF (Figure S16, Supporting Information). This value is almost identical to the capacitance measured at 0.05% P/P_0 of ethanol vapor (31.6 fF, Figure S17, Supporting Information). Consistently, similar inflection points (at the capacitance of 31.3 fF, indicated with a dash line in Figure 4e) were observed during the desorption process after repeated ethanol vapor pulses in the 0.1% to 40% P/P_0 concentration range: when the ethanol to Cu ratio is close to 1:1 (and the measured capacitance is close to 31.6 fF), the desorption slows down dramatically.

The stability of the embedded electrode is one of the primary concerns for further utilizing this device design for a wider range of materials and applications. Impressively, the response presented in Figure 4 was obtained from a device that had been stored in liquid ethanol for more than five months, with no observed detachment of the Au electrode. This device showed a similar response behavior compared to a newly fabricated one (Figure 4; Figure S19, Supporting Information). In addition, the sensor responded consistently to ethanol pulses with relative pressures ranging from 0.1% to 40%. (Figure 4e and Table S2, Supporting Information). No degradation of the sensing response was observed during a 225 h continuous ethanol sensing test at room temperature. (Figure S20, Supporting Information; see the Experimental Section for details).

3. Conclusion

We report a modified space-confined approach for synthesizing flat MOF single crystals with customizable surface patterns and electrode arrays via a one-step solvothermal reaction. Without exposing the material to hazardous chemicals or the harsh conditions commonly required for microfabrication processes, this approach enables the fabrication of surface-embossed micropatterns and surface-embedded gold electrodes as small as 5 µm on the surface of fragile MOF single crystals. The surface-embossed HKUST-1 single crystals have the potential to function as diffraction gratings, facilitating optical applications of MOF single crystals. Additionally, with this approach, we fabricated an integrated capacitive gas sensor on an HKUST-1 single crystal that reveals the effect of the coordination state of the Cu^{2+} sites on the diffusion rate of ethanol. The surface-embedded electrodes exhibited remarkable stability during both five months of storage in ethanol and 225 h of continuous sensing. This work presents a novel approach for integrating fragile MOF single crystals into miniaturized electronic devices. A future study investigating our strategy on a wider range of materials is envisioned, rendering single crystal-based devices more accessible to both academic research and practical application.

4. Experimental Section

Materials: All chemicals were ordered from commercial suppliers and used without further purification. Hydrofluoric acid (HF acid, 48%) was purchased from VWR Chemicals BDH. Copper (II) nitrate trihydrate ($Cu(NO_3)_2{\cdot}3H_2O$, 99%), dimethylformamide (DMF, 99.5%), zinc nitrate hexahydrate ($Zn(NO_3)_2{\cdot}6H_2O$, 99%), 2-methylimidazole (99%), sodium formate (HCOONa, 99%), methanol (99.9%), and glacial acetic acid (99+%) were purchased from Acros Organics. 1,3,5-Benzenetricarboxylic acid (H_3BTC, 99%) was purchased from J&K Scientific. Dimethyl sulfoxide (DMSO, 99.99%) was purchased from MicroChemicals. TI 35E, S1818, and Lor 10b photoresists were purchased from Micro Resist Technology. Schott D263 glass slides were purchased from Drix NV.

Fabrication of Patterns on the Glass Substrate via HF Etching: All microfabrication was conducted in the KU Leuven Nanocenter cleanroom facility (Class 1000). The glass slide was pre-baked on a hotplate at 160 °C for 5 min, followed by spin-coating TI 35E photoresist at 3000 rpm (revolutions per minute) for 30 s. The glass slide was then baked on the hotplate at 95 °C for 2 min. The slide was then covered by a photomask and exposed to 140 mJ cm^{-2} of 312 nm UV light, after that the glass slide was kept at room temperature for 10 min for relaxation. The glass slide was then baked on the hotplate at 120 °C for 2 min to cross-link the exposed area, making them insoluble in the developer (reversal bake). The glass slide was then exposed under 500 mJ cm^{-2} of 312 nm UV light without the mask and developed in AZ 351B developer to form the desired photoresist patterns. The glass slide was then baked on the hotplate at 150 °C for 2 min to harden the photoresist. Protected by the photoresist layer, the glass slide was etched in HF acid (25%) for

20 s to form the surface-embossed patterns. The etching speed for the Schott D263 glass was ≈5 µm min^{-1}.

Fabrication of Metal Patterns on the Glass Substrate: To fabricate Ti/Au patterns, positive photoresist S1818 was spin-coated on the glass substrate at 3000 rpm for 30 s and baked on a hotplate at 100 °C for 2 min. After exposing the photomask-covered substrate to 30 mJ cm^{-2} of 312 nm UV light and developing it in AZ 351B developer, the photoresist layer was patterned. Then, titanium and gold were deposited by magnetron sputtering. The sputtering parameters were 2×10^{-3} mbar pressure and 70 sccm of Ar flow, and the radio frequency (RF) power for the Ti and Au sputtering was 200 and 80 W, respectively. The deposition time was 30 s for 5 nm of Ti and 2 min for 120 nm of Au. Finally, the substrate was washed with acetone in an ultrasonic bath to lift off the photoresist, then cleaned with deionized water and dried with compressed air.

For the Au pattern, due to the weak adhesion between Au and the glass substrate, the ultrasonic bath would lead to the metal layer peeling off. Therefore, the lift-off process was conducted by combining Lor 10b and S1818 positive photoresist. Lor 10b was first spin-coated on the substrate at 4000 rpm for 30 s and baked on a hotplate at 180 °C for 5 min. After that, positive photoresist S1818 was spin-coated at 3000 rpm for 30 s and baked on a hotplate at 100 °C for 2 min. After exposing the photomask-covered substrate to 30 mJ cm^{-2} of 312 nm UV light and developing in AZ 351B developer, the Lor 10b and Sl818 photoresist layers were patterned. After gold deposition, the substrate was immersed in DMSO overnight to complete the lift-off process, and then cleaned with deionized water and dried with compressed air.

Synthesis of Flat HKUST-1 Single Crystal and Large HKUST-1 Single Crystal: Glass slides with and without metal patterns were covered by a second glass substrate, with two pieces of double-sided Kapton tape as spacers in between to form a space-confined mold. The flat single crystals were synthesized as in previous work to obtain large single crystals.[34] Copper nitrate trihydrate ($Cu(NO_3)_2{\cdot}3H_2O$, 0.98 g) was dissolved in a mixture of 6 mL deionized water and 6 mL DMF. Benzene-1,3,5-tricarboxylic acid (H_3BTC, 0.48 g) was mixed with 6 mL of ethanol and heated at 60 °C for 30 mins to dissolve completely. Then, the H_3BTC solution was added into the $Cu(NO_3)_2{\cdot}3H_2O$ solution, followed by adding 24 mL of glacial acetic acid. The space-confined reactors were immersed in the precursor solution in a 100 mL Schott bottle. The precursor solution in the Schott bottle provides a supply of reactants to ensure the continuous growth of the HKUST-1 single crystals. The Schott bottle was placed in a synthesis oven at 55 °C for 3 days. After the synthesis, the whole assembly was soaked in ethanol for at least 5 days, and the assembly was dried in air to evaporate the ethanol in the space between the two glass slides. Next, the space-confined reactor was opened by separating the two glass slides. Most of the patterned and electrode-embedded single crystals remained attached to the glass slide with the patterned surface. The single crystals were detached from the surface by very carefully pushing them off with a soft bristle (obtained from a tube brush), as the single crystals are very fragile (see the broken top-right corner of the crystal in Figure 3b). Flat single crystals with different morphology features were obtained in the corresponding space-confined reactors.

The crystals were picked under a microscope to find suitable samples for measurement. Exposure to ambient air was unavoidable in our current laboratory. The selected crystals were treated carefully, as conventional processing can damage them, such as evacuation (Figure S14a,b Supporting Information), gentle heating (Figure S14c,d, Supporting Information), and metal deposition via sputtering (Figure S10, Supporting Information). Even when the crystals were transferred suddenly from ambient air (relative humidity 45%) to an N_2 atmosphere, an immediate collapse was observed (Figure S15, Supporting Information). Therefore, no thermal activation was conducted before the capacitive measurements.

The large HKUST-1 single crystals in Figure S3c (Supporting Information) were synthesized with the same recipe without using the space-confined template.

Synthesis of HKUST-1 Powder: HKUST-1 powder with a crystal size of ≈500 nm was synthesized following a reported protocol.[48] $Cu(NO_3)_2{\cdot}3H_2O$ (1.2 g dissolved in 10 mL ethanol) was mixed with H_3BTC (0.6 g dissolved in 10 mL ethanol), and stirred for 24 h at room temperature. After synthesis, the HKUST-1 powder was washed with ethanol to remove unreacted precursors and dried in air before use.

Synthesis of ZIF-8 Single Crystals: The ZIF-8 single crystals were synthesized as in previous work to obtain large single crystals.[39] 1.764 g (5.93 mmol) of zinc nitrate hexahydrate was dissolved in 15 mL of methanol. 0.9739 g (11.86 mmol) of 2-methylimidazole, and 0.4034 g (5.93 mmol) of sodium formate were dissolved in 25 mL of methanol. The two solutions were mixed and stirred for 5 min at room temperature. The precursor solution was filtered through a 0.2 µm polytetrafluoroethylene (PTFE) syringe filter. The space-confined reactors were immersed in the precursor solution in a 100 mL Schott bottle. The Schott bottle was placed in a synthesis oven at 90 °C for 24 h. After the synthesis, the ZIF-8 single crystals were washed and soaked in ethanol for further characterizations.

Micrographs, SEM Images, and Optical Profilometry: The micrographs of samples were recorded using a LEICA DM 8000M microscope. Scanning electron microscopy images were recorded using a JEOL JSM-6010LV microscope. The crystals in Figure S3 (Supporting Information) were placed on a glass substrate, and the powder crystals in Figure S18 (Supporting Information) were deposited on carbon tape. 2 nm of Au/Pt was sputter-coated on the samples before SEM imaging. The optical profilometry of the crystals was recorded on a Sensofar 3D optical profilometer.

X-Ray Diffraction: Diffractograms of oriented HKUST-1 single crystals were obtained using a Malvern PANalytical Empyrean diffractometer in Bragg-Brentano geometry, equipped with a Cu anode operating at 45 kV and 40 mA and PIXcel3D solid-state detector. The samples were placed on a movable flat stage, and their position was adjusted with a top alignment camera to ensure that the beam landed on the single crystals. The incident beam path optics were adjusted for a beam size of ≈7.4 mm × 4.8 mm at low angles. Gonio mode measurements were then performed in a 5°–45° 2θ range with a step size of 0.0131° and a counting time of 1000 s.

Physisorption: Ethanol physisorption of HKUST-1 powder was performed using a Micromeritics 3Flex 3500 instrument at 25 °C. Samples were activated at 130 °C under dynamic vacuum (1×10^{-6} mbar) for 6 h. A custom isotherm program was developed in order to replicate the partial pressure dosing monitored during capacitance measurements with single vapor pulses. Extended equilibration time intervals of 2500s, and relative pressure fluctuations of 0.001% were employed as equilibrium conditions at each point of the isotherm in order to allow sufficient time for EtOH diffusion in the HKUST-1 powder.

Capacitive Gas Sensing: The single-crystal capacitive gas sensors were measured using a probe station equipped with an impedance analyzer (Zurich Instruments MFIA) at a frequency of 100 kHz and a voltage of 0.5 V. The 100 kHz measurement frequency was chosen to avoid the spurious contributions that occur at low frequencies and high loadings, presumably due to electrode polarization effects.[49] The single-crystal device (thickness of ≈20 µm) was placed in a test box with a gas inlet and outlet (Figure S21, Supporting Information). The glass window on the top was used to monitor the contact of the electrode on the crystal and the probes, and to observe the changes of the crystal during sensing. Through the opening on the two sides of the box, the crystal was contacted with the external probes, which were wrapped tightly by a rubber membrane cut from laboratory nitrile gloves. The glove fingers were used: the wide side was glued to the box, the narrow side was used to wrap the probe arm to ensure sealing while leaving sufficient leeway for the probe to be adjusted. The capacitance of the open circuit of the instrument was measured to be ≈37.2 fF (this value was measured by placing the two probes close to the interdigitated electrodes on the crystal, but without touching them). This value was subtracted in the calculation of the capacitance of the single crystal sensor. The gas flow was controlled by mass flow controllers (MFCs) via a LabVIEW interface.

To make a consistent comparison for different ethanol vapor concentrations and to avoid damage to the single crystal by the movement of the probes, the capacitance data were extracted from a continuous

measurement run lasting over 225 h. The following sequence was used:1) the single-crystal device was first purged with ethanol vapor (40% P/P_0) for 10 min to replace the moisture in the pores of HKUST-1. 2) Pure N_2 was purged for 26 h to activate the single-crystal device as much as possible. 3) Ethanol vapor with concentrations ranging from 0% to 80% P/P_0 was dosed over 19 h. 4) Pure N_2 was purged for 3 h. 5) Ethanol vapor pulses with a concentration of 0.1%, 1%, and 10% P/P_0 were dosed for 27 h, followed by continuous 40% P/P_0 of ethanol pulses dosing for 150 h.

Statistical Analysis: The results in Figure 4c ($\Delta C/C_0$),d,e and Figures S16, S17, and S20 (Supporting Information) were measured on the same device. The normalized capacitances (Figure 4d) were extracted from Figure S17 (Supporting Information), which shows the raw data of the real-time capacitive response.

Supporting Information

Supporting Information is available from the Wiley Online Library or from the author.

Acknowledgements

The authors acknowledge the funding by the Research Foundation Flanders (FWO Vlaanderen) in research projects G087422N, G085720N, and 1121221N, and the funding by KU Leuven in research projects C14/20/085, C32/18/056, PDM/20/114. M.T. acknowledges financial support by the National Key R&D Program of China (2021YFB3200800) and the Shanghai Pujiang Program (21PJ1415200). V.R.-G. thanks FWO for a Marie Skłodowska Curie Actions—Seal of Excellence and a Junior Postdoctoral Fellowships (12Z6520N and 1263622N).

[1] S. Furukawa, J. Reboul, S. Diring, K. Sumida, S. Kitagawa, *Chem. Soc. Rev.* **2014**, *43*, 5700.
[2] L. Feng, K.-Y. Wang, J. Powell, H.-C. Zhou, *Matter* **2019**, *1*, 801.
[3] J.-R. Li, R. J. Kuppler, H.-C. Zhou, *Chem. Soc. Rev.* **2009**, *38*, 1477.
[4] M. Ding, R. W. Flaig, H.-L. Jiang, O. M. Yaghi, *Chem. Soc. Rev.* **2019**, *48*, 2783.
[5] T. Rodenas, I. Luz, G. Prieto, B. Seoane, H. Miro, A. Corma, F. Kapteijn, F. X. Llabrés i Xamena, J. Gascon, *Nat. Mater.* **2015**, *14*, 48.
[6] Q. Wang, D. Astruc, *Chem. Rev.* **2020**, *120*, 1438.
[7] C. A. Trickett, T. M. Osborn Popp, J. Su, C. Yan, J. Weisberg, A. Huq, P. Urban, J. Jiang, M. J. Kalmutzki, Q. Liu, J. Baek, M. P. Head-Gordon, G. A. Somorjai, J. A. Reimer, O. M. Yaghi, *Nat. Chem.* **2019**, *11*, 170.
[8] C. He, D. Liu, W. Lin, *Chem. Rev.* **2015**, *115*, 11079.
[9] L. E. Kreno, K. Leong, O. K. Farha, M. Allendorf, R. P. Van Duyne, J. T. Hupp, *Chem. Rev.* **2012**, *112*, 1105.
[10] W.-T. Koo, J.-S. Jang, I.-D. Kim, *Chem* **2019**, *5*, 1938.
[11] J.-H. Dou, M. Q. Arguilla, Y. Luo, J. Li, W. Zhang, L. Sun, J. L. Mancuso, L. Yang, T. Chen, L. R. Parent, G. Skorupskii, N. J. Libretto, C. Sun, M. C. Yang, P. V. Dip, E. J. Brignole, J. T. Miller, J. Kong, C. H. Hendon, J. Sun, M. Dincă, *Nat. Mater.* **2021**, *20*, 222.
[12] A. Fuchs, P. Mannhardt, P. Hirschle, H. Wang, I. Zaytseva, Z. Ji, O. Yaghi, S. Wuttke, E. Ploetz, *Adv. Mater.* **2021**, 2104530.
[13] Y. Miao, M. Tsapatsis, *Chem. Mater.* **2021**, *33*, 754.
[14] M. Tu, B. Xia, D. E. Kravchenko, M. L. Tietze, A. J. Cruz, I. Stassen, T. Hauffman, J. Teyssandier, S. De Feyter, Z. Wang, R. A. Fischer, B. Marmiroli, H. Amenitsch, A. Torvisco, M. d. J. Velásquez-Hernández, P. Falcaro, R. Ameloot, *Nat. Mater.* **2021**, *20*, 93.
[15] L. Li, J. Liu, M. Zeng, L. Fu, *Nano Res.* **2021**, *14*, 1609.
[16] W. Yu, F. Li, L. Yu, M. R. Niazi, Y. Zou, D. Corzo, A. Basu, C. Ma, S. Dey, M. L. Tietze, U. Buttner, X. Wang, Z. Wang, M. N. Hedhili, C. Guo, T. Wu, A. Amassian, *Nat. Commun.* **2018**, *9*, 5354.
[17] Y. Liu, Y. Zhang, Z. Yang, H. Ye, J. Feng, Z. Xu, X. Zhang, R. Munir, J. Liu, P. Zuo, Q. Li, M. Hu, L. Meng, K. Wang, D.-M. Smilgies, G. Zhao, H. Xu, Z. Yang, A. Amassian, J. Li, K. Zhao, S. Liu, *Nat. Commun.* **2018**, *9*, 5302.
[18] Z. Gu, Z. Huang, C. Li, M. Li, Y. Song, *Sci. Adv.* **2018**, *4*, eaat2390.
[19] W. Li, X. Wang, J. Liao, Y. Jiang, D. Kuang, *Adv. Funct. Mater.* **2020**, *30*, 1909701.
[20] Y.-X. Chen, Q.-Q. Ge, Y. Shi, J. Liu, D.-J. Xue, J.-Y. Ma, J. Ding, H.-J. Yan, J.-S. Hu, L.-J. Wan, *J. Am. Chem. Soc.* **2016**, *138*, 16196.
[21] D.-G. Ha, M. Rezaee, Y. Han, S. A. Siddiqui, R. W. Day, L. S. Xie, B. J. Modtland, D. A. Muller, J. Kong, P. Kim, M. Dincă, M. A. Baldo, *ACS Cent. Sci.* **2021**, *7*, 104.
[22] S. Guthrie, L. Huelsenbeck, A. Salahi, W. Varhue, N. Smith, X. Yu, L. U. Yoon, J. J. Choi, N. Swami, G. Giri, *Nanoscale Adv* **2019**, *1*, 2946.10.1039.C9NA00254E.
[23] A. Sorrenti, L. Jones, S. Sevim, X. Cao, A. J. deMello, C. Martí-Gastaldo, J. Puigmartí-Luis, *J. Am. Chem. Soc.* **2020**, *142*, 9372.
[24] R. Ameloot, E. Gobechiya, H. Uji-i, J. A. Martens, J. Hofkens, L. Alaerts, B. F. Sels, D. E. De Vos, *Adv. Mater.* **2010**, *22*, 2685.
[25] S. Guthrie, L. Huelsenbeck, A. Salahi, W. Varhue, N. Smith, X. Yu, L. U. Yoon, J. J. Choi, N. Swami, G. Giri, *Nanoscale Adv* **2019**, *1*, 2946.
[26] J. Zhang, Q. Guo, X. Li, C. Li, K. Wu, I. Abrahams, H. Yan, M. M. Knight, C. J. Humphreys, L. Su, *ACS Nano* **2020**, *14*, 11029.
[27] Y. Lei, Y. Chen, Y. Gu, C. Wang, Z. Huang, H. Qian, J. Nie, G. Hollett, W. Choi, Y. Yu, N. Kim, C. Wang, T. Zhang, H. Hu, Y. Zhang, X. Li, Y. Li, W. Shi, Z. Liu, M. J. Sailor, L. Dong, Y.-H. Lo, J. Luo, S. Xu, *Adv. Mater.* **2018**, *30*, 1705992.
[28] L. Sun, S. S. Park, D. Sheberla, M. Dincă, *J. Am. Chem. Soc.* **2016**, *138*, 14772.
[29] M. L. Aubrey, B. M. Wiers, S. C. Andrews, T. Sakurai, S. E. Reyes-Lillo, S. M. Hamed, C.-J. Yu, L. E. Darago, J. A. Mason, J.-O. Baeg, F. Grandjean, G. J. Long, S. Seki, J. B. Neaton, P. Yang, J. R. Long, *Nat. Mater.* **2018**, *17*, 625.
[30] T. Makita, A. Yamamura, J. Tsurumi, S. Kumagai, T. Kurosawa, T. Okamoto, M. Sasaki, S. Watanabe, J. Takeya, *Sci. Rep.* **2020**, *10*, 4702.
[31] X. Feng, M. A. Meitl, A. M. Bowen, Y. Huang, R. G. Nuzzo, J. A. Rogers, *Langmuir* **2007**, *23*, 12555.
[32] S. Sachdeva, M. R. Venkatesh, B. E. Mansouri, J. Wei, A. Bossche, F. Kapteijn, G. Q. Zhang, J. Gascon, L. C. P. M. de Smet, E. J. R. Sudhölter, *Small* **2017**, *13*, 1604150.

[33] S. S. Chui, S. M.-F. Lo, J. P. H. Charmant, A. G. Orpen, I. D. Williams, *Science* **1999**, *283*, 1148.
[34] T. M. Tovar, J. Zhao, W. T. Nunn, H. F. Barton, G. W. Peterson, G. N. Parsons, M. D. LeVan, *J. Am. Chem. Soc.* **2016**, *138*, 11449.
[35] Z.-G. Gu, A. Pfriem, S. Hamsch, H. Breitwieser, J. Wohlgemuth, L. Heinke, H. Gliemann, C. Wöll, *Micropor. Mesopor. Mat.* **2015**, *211*, 82.
[36] J. Wu, J. Chen, C. Wang, Y. Zhou, K. Ba, H. Xu, W. Bao, X. Xu, A. Carlsson, S. Lazar, A. Meingast, Z. Sun, H. Deng, *Adv. Sci.* **2020**, *7*, 1903003.
[37] Q. Liu, J.-M. Yang, L.-N. Jin, W.-Y. Sun, *CrystEngComm* **2016**, *18*, 4127.
[38] K. S. Park, Z. Ni, A. P. Côté, J. Y. Choi, R. Huang, F. J. Uribe-Romo, H. K. Chae, M. O'Keeffe, O. M. Yaghi, *Proc. Natl. Acad. Sci. U.S.A.* **2006**, *103*, 10186.
[39] C. Chen, A. Ozcan, A. O. Yazaydin, B. P. Ladewig, *J. Membr. Sci.* **2019**, *575*, 209.
[40] Z. Wang, A. Syed, S. Bhattacharya, X. Chen, U. Buttner, G. Iordache, K. Salama, T.h. Ganetsos, E. Valamontes, A. Georgas, I. Raptis, P. Oikonomou, A. Botsialas, M. Sanopoulou, *Microelectron. Eng.* **2020**, *225*, 111253.
[41] C. Prestipino, L. Regli, J. G. Vitillo, F. Bonino, A. Damin, C. Lamberti, A. Zecchina, P. L. Solari, K. O. Kongshaug, S. Bordiga, *Chem. Mater.* **2006**, *18*, 1337.
[42] M. D. Allendorf, R. J. T. Houk, L. Andruszkiewicz, A. A. Talin, J. Pikarsky, A. Choudhury, K. A. Gall, P. J. Hesketh, *J. Am. Chem. Soc.* **2008**, *130*, 14404.
[43] J. R. Álvarez, E. Sánchez-González, E. Pérez, E. Schneider-Revueltas, A. Martínez, A. Tejeda-Cruz, A. Islas-Jácome, E. González-Zamora, I. A. Ibarra, *Dalton Trans.* **2017**, *46*, 9192.
[44] Z. Zhai, X. Zhang, X. Hao, B. Niu, C. Li, *Adv. Mater. Technol.* **2021**, *6*, 2100127.
[45] J. Kärger, T. Binder, C. Chmelik, F. Hibbe, H. Krautscheid, R. Krishna, J. Weitkamp, *Nat. Mater.* **2014**, *13*, 333.
[46] W. Zhou, C. Wöll, L. Heinke, *Materials* **2015**, *8*, 3767.
[47] A. S. Babal, A. K. Chaudhari, H. H. -M. Yeung, J. Tan, *Adv. Mater. Interfaces* **2020**, *7*, 2000408.
[48] L. H. Wee, M. R. Lohe, N. Janssens, S. Kaskel, J. A. Martens, *J. Mater. Chem.* **2012**, *22*, 13742.
[49] P. B. Ishai, M. S. Talary, A. Caduff, E. Levy, Y. Feldman, *Meas. Sci. Technol.* **2013**, 22.